ACS Catalysis

pubs.acs.org/acscatalysis Research Article

Modulation of Schottky Barrier Height and Electronic Structure in Transition-Metal@Nitrogen-Doped-Carbon Core−Shell Cocatalysts Loaded with $Mn_xCd_{1-x}S$ Nanorods for Enhanced Photocatalytic Hydrogen Evolution

Yufeng Li,[‖] Songqing Zhang,[‖] Chunmei He, Hongxia Yao, Changfa Guo,* Wentao Wang,* and Yong Hu*

Cite This: *ACS Catal.* 2025, 15, 2315−2327 Read Online

ACCESS | Metrics & More | Article Recommendations | Supporting Information

ABSTRACT: Transition-metal (TM)/carbon nanocomposites have emerged as a type of low-cost high-efficiency photocatalysis cocatalyst for their high photoactivity comparable to typical noble metals such as Pt. However, the underlying cocatalytic mechanism in this combined nanoscaled system has not been understood sufficiently. In this work, a core−shell nanoparticle (NP) cocatalyst has been designed and synthesized by using three kinds of large-work-function TMs (Co, Ni, and Cu) and nitrogen-doped carbon (NC) to construct a core−shell structure (TM@NC), and its photocatalytic hydrogen evolution performance has been studied with $Mn_xCd_{1-x}S$ nanorods (NRs). It has been found that the TMs endow the TM@NC NPs with large work functions, which act as efficient electron traps. Significantly, the Schottky barrier height at the interface of TM@NC and $Mn_xCd_{1-x}S$ can be modulated by the embedded TMs, and therefore the transfer efficiency of the photoelectrons can be adjusted. Thus, the relationships between photoactivity and the Schottky barrier height can be obtained. The NC layer in the TM@NC structure not only protects the embedded TMs from overoxidation but also provides abundant catalytic sites for hydrogen evolution reaction. Meanwhile, the electronic structure of the NC layer can be refined by the embedded TMs as well, favoring the release of hydrogen from its surface. As a result, all the TM@NC NP cocatalysts exhibit comparable cocatalytic activity to optimized Pt NPs, and the Ni@NC sample obviously outperforms Pt. This work highlights the effect of the Schottky barrier in adjusting the photocatalytic activity and provides deep insight into the photoactivity engineering of photocatalysts by incorporating TMs with semiconductor materials.

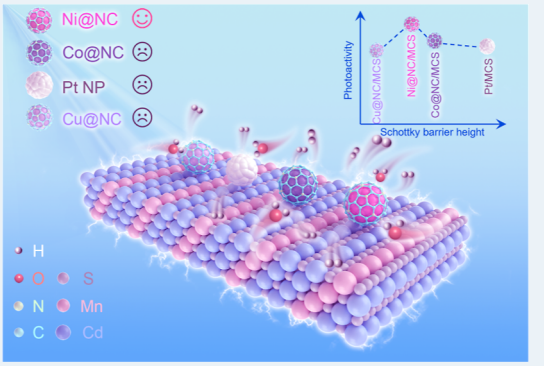

KEYWORDS: *$Mn_xCd_{1-x}S$ nanorods, nitrogen-doped carbon, transition metals, Schottky barrier, photocatalytic hydrogen evolution*

INTRODUCTION

Photocatalytic water splitting is one of the most desirable approaches to supply hydrogen (H_2) as a clean energy carrier for maintaining carbon neutrality.[1,2] The major challenge this technology faces is low solar-to-hydrogen (STH) conversion efficiency of semiconductor photocatalysts, which is limited by interconnected multiple factors, including insufficient light harvesting, severe recombination of photogenerated carriers, and sluggish reaction kinetics.[3] Among them, the recombination problem is particularly concerned since over 90% of carriers quench in bulk without the assistance of any modification strategies,[4,5] which is the most critical origin of low STH efficiency for wide-spectral-response photocatalysts.

To accelerate electron transfer from the bulk to the surface of a semiconductor photocatalyst, metal nanoparticles (NPs) with a large work function (Φ) are often loaded onto the semiconductor surface to form a Schottky barrier, where metal NPs play the role of electron wells, allowing energetic electrons to flow into metal NPs from the excited semiconductors while suppressing the counterflow. In this regard, the noble metals (Pt, Pd, and Au) have larger Φ (>5.2 eV) and chemical stability among various metals and endow most semiconductors with obviously enhanced photocatalytic activity toward H_2 evolution reaction (HER).[6] However, the high cost of the noble metals has stimulated research interests in looking into alternatives to them. It was reported that non-noble transition metals (TMs) including Co, Ni, and Cu and even carbon nanomaterials such as nanotubes and graphene are

Received: October 22, 2024
Revised: December 29, 2024
Accepted: January 13, 2025

https://doi.org/10.1021/acscatal.4c06476
ACS Catal. 2025, 15, 2315−2327

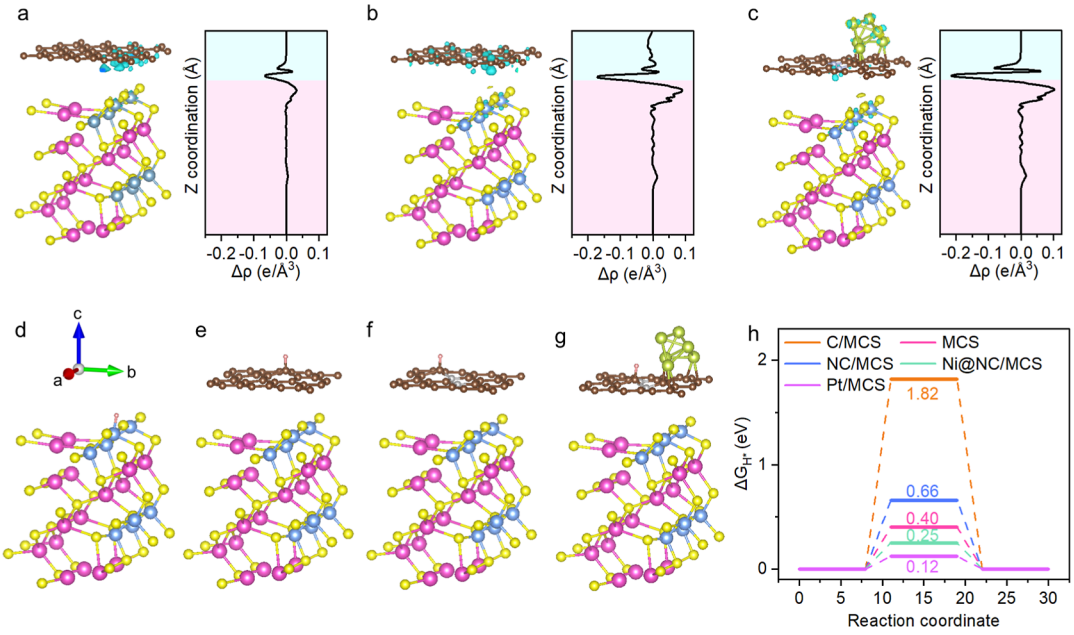

Figure 1. Models and calculated $\Delta\rho$ for (a) C/MCS, (b) NC/MCS, and (c) Ni@NC/MCS. Models for H* adsorption on (d) MCS, (e) C/MCS, (f) NC/MCS, and (g) Ni@NC/MCS, and (h) ΔG_{H^*} on MCS, C/MCS, NC/MCS, Ni@NC/MCS, and Pt/MCS. All the MCS models have an x value of 0.35. The Ni, C, N, Mn, Cd, S, and H atoms are represented by army green, brown, gray, steel blue, rose-Bengal, yellow, and light pink balls, respectively.

potential candidate cocatalysts for photocatalytic HER.[6,7] These TMs have larger Φ (5.0 eV for Co polycrystalline, 4.53−5.10 and 5.04−5.35 eV for different Cu and Ni facets, respectively), second only to the above noble metals, but suffer from inactivation because of easy oxidation.[6] The carbon materials have the cost advantage over all metals and good electric conductivity but suffer from a low ability of trapping electrons due to smaller Φ (4.42 eV for graphene).[6] As a compromise, carbon-based nanocomposites made of carbon and TMs were proposed as effective cocatalysts for photocatalytic HER.[8−13] For example, Song et al. reported Ni@carbon (Ni@C) core−shell nanospheres as cocatalysts of CdS nanorods (NRs) for boosting HER by the nanoconfined effect of Ni@C.[9] Ding et al. proposed Co@nitrogen-doped carbon (Co@NC) core−shell nanospheres as cocatalysts of CdS NRs for boosting HER through electron transfer between CdS and Co@NC.[10] Liu et al. reported Ni@NC NPs as active and stable H_2 evolution cocatalysts for photocatalytic overall water splitting over $SrTiO_3$, paying special attention to the roles of NC and the influence of N dopants on the electronic structure of active sites rather than the influence of various embedded metals.[13] In short, the working mechanism of TM@NC-decorated semiconductors has not been sufficiently revealed, such as the effect of Schottky barrier height on carrier separation, specific carrier migration kinetics, and refinement of the electronic structure of catalytic sites for HER kinetics. Furthermore, all of Co, Ni, and Cu metals with Φ close to the above noble metals hold potential to act as main components of high-efficiency carbon-based cocatalysts. However, the applicability of such cocatalysts with different TMs for improving the photocatalytic efficiency has rarely been reported.

The influence of Schottky barrier height on photoactivity has been investigated in terms of two type of Schottky junctions in the previous reports based on one or two at most reference samples.[14−25] The first type refers to those in which photoelectrons transfer from a plasmonic metal to a semiconductor under irradiation. For this type, it has been recognized that a lower Schottky barrier height favors the electron transfer process and enhances photocatalytic activity.[16−18] However, there is no consistent understanding obtained on the influence for the popular second type of Schottky junctions in which photoelectrons transfer from semiconductors to metals under irradiation. Specifically, some of them argued that a higher Schottky barrier height is helpful for photogenerated carrier separation.[19,20] On the contrary, the others suggested that a lower Schottky barrier height favors carrier separation.[21,22] Furthermore, Schottky barrier height depends on the Fermi level (E_F) difference between semiconductor and metal, and Φ is sensitive to a specific crystal facet and even grain size of nanomaterials.[22,23] However, some reports suffer from a lack of powerful experimental evidence for the determination of Φ,[20,22,24,25] increasing the uncertainty of conclusions on the influence of Schottky barrier height. In addition, the previous studies on the second type of Schottky junctions are focused on noble metals rather than TM-carbon composites.[16−18,23−29,] Collectively, the influence of the Schottky barrier height on photoactivity remains controversial, which needs to be clarified by a systematic study dealing with multiple control experiments.

Herein, we first examined the theoretical validity of TM@NC (TM = Co, Ni, Cu, respectively) NPs acting as efficient cocatalysts of $Mn_xCd_{1-x}S$ (MCS) NRs for boosting the photocatalytic HER by employing density functional theory (DFT). In this case, MCS was selected as a model catalyst due to its adjustable enough negative conduction band minima (CBM) suitable for water reduction and light-harvesting ability in the ultraviolet−visible region,[30,31] making it a good candidate semiconductor for examining the effect of Schottky barrier height on photocatalytic H_2 evolution in the full spectrum and visible region, respectively. Taking Ni@NC as a representative example, the side views of charge density

https://doi.org/10.1021/acscatal.4c06476
ACS Catal. 2025, 15, 2315−2327

difference ($\Delta\rho$) for carbon layer-loaded MCS (C/MCS), NC layer-loaded MCS (NC/MCS), and Ni@NC-loaded MCS (Ni@NC/MCS) are present in Figure 1, where x was fixed at 0.35 since it gives rise to the highest photocatalytic HER activity in the range of x = 0−1 for bare MCS NRs (Figure S1). All of the following MCS-based heterojunctions correspond to an x value of 0.35 unless otherwise stated. The charge density difference reveals an electronic interaction between the carbon layer and MCS (Figure 1a), and the interfacial interaction is enhanced upon introducing N elements into the carbon layer (Figure 1b). Meanwhile, the N dopants provide abundant coordination sites binding metal NPs.[32] The introduction of Ni clusters slightly weakens the electronic interaction, which remains obviously stronger than that of the C/MCS (Figure 1c). Notably, the presence of Ni clusters remarkedly promotes the density of state (DOS) around E_F (Figure S2), helping to improve charge-transfer kinetics at the electrode/electrolyte interface, which is a fundamental factor affecting photoelectric conversion efficiency.[33,34] Furthermore, bare MCS shows strong adsorption to the hydrogen intermediate (H*) on its surface (Figure 1d−h). With the NC layer as a cocatalyst of MCS, the adsorption site is transferred from MCS to the NC layer with an obviously reduced adsorption free energy (ΔG_{H^*}). After Ni clusters are loaded into the NC layer, the electronic structure of NC is refined such that the ΔG_{H^*} over Ni@NC/MCS is further reduced to 0.25 eV lower than that of MCS and is the closest to that of Pt/MCS (Figure S3), displaying good potential in boosting HER. To verify the above analysis, we synthesized TM@NC (TM = Co, Ni, and Cu) NP-loaded MCS hetero-NRs (HNRs) by a three-step method. It was found that all the TM@NC NPs have Φ close to that of Pt NPs, and the Schottky barrier height between TM@NC NPs and MCS NRs depends on the specific metals, which plays a vital role in the reconciliation of electron flow forward and backward between the two components. As a result, all the TM@NC NPs exhibit comparable cocatalytic HER activity compared to optimized Pt NPs. In particular, the Ni@NC significantly outperforms Pt.

EXPERIMENTAL SECTION

Chemicals. The chemicals cobaltous nitrate hexahydrate [$Co(NO_3)_2{\cdot}6H_2O$, ≥99%], nickel nitrate hexahydrate [$Ni(NO_3)_2{\cdot}6H_2O$, AR], cupric nitrate trihydrate [$Cu(NO_3)_2{\cdot}3H_2O$, AR], manganous acetate tetrahydrate [$Mn(CH_3COO)_2{\cdot}4H_2O$, AR], sodium sulfate ($Na_2SO_4$, AR), sodium sulfite ($Na_2SO_3$, AR), sodium borohydride ($NaBH_4$, AR), glucose ($C_6H_{12}O_6$, AR), thioacetamide (CH_3CSNH_2, AR), absolute ethanol (AR), and ethylenediamine (AR) were purchased from Sinopharm Chemical Reagent Co., Ltd. (China). Dicyandiamide ($C_2H_4N_4$, CP) and cadmic acetate dihydrate [$Cd(CH_3COO)_2{\cdot}2H_2O$, AR] were purchased from Shanghai Zhanyun Chemical Co., Ltd. Sodium sulfide (Na_2S, 98%) and chloroplatinic acid hexahydrate ($H_2PtCl_6{\cdot}6H_2O$, AR, Pt ≥ 37.5%) were purchased from J&K Scientific and Shanghai Aladdin Biochemical Technology Co., Ltd. (China), respectively. All of the above chemicals were directly used without further purification, and deionized water (1.2 μS cm^{-1}) was used throughout this work.

Preparation of Catalysts. TM@NC NPs were synthesized according to the previous literature.[35] 0.2 g of $C_6H_{12}O_6$ and 1.0 g of $C_2H_4N_4$ were dissolved in 10 mL of deionized water with stirring for 30 min. The solution was transferred to a 25 mL Teflon-lined stainless-steel autoclave and was then heated and kept at 200 °C for 6 h in a drying oven. The resultant mixture was filtered through a 0.22 μm membrane to remove large particles for obtaining a red-brown suspension. Subsequently, 1 mmol of metal nitrate [$Ni(NO_3)_2{\cdot}6H_2O$, $Co(NO_3)_2{\cdot}6H_2O$, and $Cu(NO_3)_2{\cdot}3H_2O$, respectively] was added in the suspension with stirring for 30 min; the obtained mixture was then evaporated to dryness to collect TM^{2+}-NC quantum dots (NCQDs) powder. Finally, the TM@NC NPs were obtained by annealing the TM^{2+}-NCQDs powder in an N_2 atmosphere at 600 °C for 2 h with a heating rate of 5 °C min^{-1}. The dosage of $Ni(NO_3)_2{\cdot}6H_2O$ was varied as 0.5, 1, and 2 mmol to optimize the Ni content in Ni@NC; the obtained samples were denoted as Ni@NC-L, Ni@NC, and Ni@NC-M with an actual Ni content of 0.9, 2.2, and 3.5 wt %, respectively, which were determined by atomic absorption spectroscopy. To adjust the percentage of the Ni^{2+} oxidation state in Ni@NC, the double dosage of $Ni(NO_3)_2{\cdot}6H_2O$ and NCQDs was used to obtain Ni^0@NC NPs with a lower percentage of the Ni^{2+} oxidation state. Moreover, the Ni@NC NPs were calcined in air at 300 °C for 30 min to obtain Ni^{2+}@NC NPs with a higher percentage of Ni^{2+} oxidation state. In addition, bare NC and NiO NPs were also synthesized by annealing pure NCQDs and $Ni(NO_3)_2{\cdot}6H_2O$ in an N_2 atmosphere at 600 °C for 2 h, respectively.

MCS NRs were obtained using a modified solvothermal method according to the previous report.[36] Typically, 3 mmol of $Mn(CH_3COO)_2{\cdot}4H_2O$, 7 mmol of $Cd(CH_3COO)_2{\cdot}2H_2O$, and 12.5 mmol of CH_3CSNH_2 were dissolved in a mixed solvent of deionized water (15 mL) and ethylenediamine (15 mL) by stirring for 30 min. The solution was then transferred into a 50 mL Teflon-lined stainless-steel autoclave and was heated at 200 °C for 24 h. After the mixture was cooled to room temperature, the yellow precipitate was collected by centrifugation, washed with deionized water and absolute ethanol several times, and dried at 80 °C under vacuum overnight.

50 mg of MCS NRs was dispersed in a mixed solvent of deionized water (50 mL) and absolute ethanol (40 mL) under ultrasonication for 30 min, marked as suspension A. Certain amounts (0.5, 1.5, 2.5, and 3.5 mg) of TM@NC NPs were suspended in 10 mL of absolute ethanol by ultrasonication for 30 min, marked as suspension B. Subsequently, suspension B was slowly added to suspension A under stirring, and the mixture was then stirred for 5 h at room temperature. Finally, the solid was collected, washed with deionized water and absolute ethanol several times, and dried at 80 °C under a vacuum overnight. The obtained sample was denoted as TM@NC/MCS-x (x = 1%, 3%, 5%, and 7%) HNRs, x represents the mass ratio of TM@NC NPs to MCS NRs. The NC/MCS-5 and NiO/MCS-5 HNRs were also synthesized under the same conditions except for the replacement of Ni@NC NPs with NC and NiO NPs, respectively.

Pt NPs were loaded on MCS NRs by using a photodeposition method. Detailly, 50 mg of MCS NRs was ultrasonically dispersed in 100 mL of aqueous solution containing 0.35 M Na_2S and 0.25 M Na_2SO_3, and different volumes of H_2PtCl_6 (5 g/L). The suspension was placed in a Pyrex top−irradiation reaction vessel with a stationary temperature of 25 °C and irradiated under full light irradiation (the detail information on irradiation can be seen in the section of photocatalytic HER tests) for 3 h. The obtained samples were denoted as Pt/MCS-x (x = 1, 2, and 3 wt %) HNRs, where x represents the mass percentage of Pt NPs.

https://doi.org/10.1021/acscatal.4c06476
ACS Catal. 2025, 15, 2315−2327

The Pt NPs were prepared through a reduction reaction of H_2PtCl_6 with $NaBH_4$. An excess of $NaBH_4$ solution (0.5 M) was added to a certain amount of H_2PtCl_6 solution (5 g/L) with stirring for 1 h. The black precipitate was collected by centrifugation, washed with deionized water and absolute ethanol several times, and dried at 80 °C under vacuum overnight.

Photocatalytic HER Tests. The photocatalytic HER tests were carried out with a gas-sealed circulation system, which was kept at 25 °C by cooling the water. The detailed configurations of the photocatalytic system and photoreactor are shown in Figure S4a,b. Typically, 10 mg of photocatalysts was dispersed in an aqueous solution (100 mL) with 0.35 M Na_2S and 0.25 M Na_2SO_3 as hole sacrificial reagents. Before light irradiation, the system was vacuumed to eliminate the air. A 300 W Xe lamp (Microsolar300, Beijing PerfectLight Technology Co., Ltd., China) was used as the light source of a full light irradiation (320 nm < λ < 780 nm, irradiation intensity: 2472.8 W m^{-2}). The irradiation intensity was determined by using an optical power meter (PL-MW2000, Beijing PerfectLight Technology Co., Ltd., China) according to a previous method.[37,38] Detailly, the distance between the probe and xenon lamp before the test was adjusted to be the same as the distance between the xenon lamp and the liquid surface in the photoreactor, as shown in Figure S5a. After fixing the distance between the xenon lamp and probe, five points were selected and measured separately and averaged. The photon distribution irradiated to the liquid surface was measured by using a PLA-20Plant Lighting Analyzer (EVERFINE Corporation, China), as shown in Figure S5b. The amount of H_2 evolution was monitored by online gas chromatography (GC-7890B) equipped with a thermal conductivity detector and Ar gas was used as the carrier gas. For cyclic tests, the reaction system was outgassed before each run, and the spent photocatalysts were recycled by centrifugation and washed with deionized water for the next run of cyclic tests.

The apparent quantum yield (AQY) of photocatalytic H_2 evolution was calculated according to the formula

$$\mathrm{AQY}\ (\%) = \frac{2 \times \text{number of evolved } H_2 \text{ molecules}}{\text{number of incident photons}} \times 100 = \frac{2 \times n_{H_2} \times N_A}{S \times P \times t \times \frac{\lambda}{h \times c}} \times 100 \quad (1)$$

where n_{H_2} is the amount of evolved H_2 molecules in the photocatalytic HER. N_A, λ, h, and c represent the Avogadro constant, monochromatic wavelength, Planck constant, and speed of light. S, P, and t are the area, light intensity, and time of irradiation, respectively.

Material Characterizations. Field-emission scanning electron microscopy (SEM, GeminiSEM 300 scanning electron microanalyzer, Japan), transmission electron microscopy (TEM, JEOL JEM-2100F, Japan), and high-resolution TEM (HRTEM) combined with selected-area electron diffraction (SAED) were applied to analyze morphology and chemical constitution of samples. The accelerating voltage is 5 kV for SEM observation and 200 kV for TEM and HRTEM. Powder X-ray diffraction (XRD, Philips PW 3040/60 X-ray diffractometer, Cu Kα radiation, scanning rate: 0.06 deg s^{-1}, Germany) was used to characterize the phase constitution of samples. The content of Ni species was detected by an atomic absorption spectrometer (TAS-990, Beijing Puxi Co., Ltd., China). X-ray photoelectron spectroscopy (XPS, ESCALab MKII X-ray photoelectron spectrometer, excitation source: Mg Kα X-ray, UK) was performed to analyze the chemical environments of the elements in the samples. Ultraviolet photoemission spectroscopy (UPS) analysis was performed with the He I (21.22 eV) emission line for excitation. The data were acquired with a bias of −10 V. UV−vis diffuse reflectance spectra (UV−vis DRS) were obtained on a Thermo Nicolet Evolution 500 UV−vis spectrophotometer (Japan) equipped with an integrating sphere attachment to investigate the light-harvesting ability of samples. Raman spectra were collected on a LabRAM HR Evolution Raman spectrometer (UK) with an excitation light of 532 nm.

Physicochemical Measurements. Steady-state photoluminescence (PL) spectra and time-resolved PL spectra (TRPL) were acquired on an FLS 920 and FLS 980 fluorescence spectrophotometer (UK), respectively, with an excitation wavenumber of 350 nm. The contact angle measurements were performed via an optical contact angle measuring device (OCAH200, Dataphysics, Germany). Mott−Schottky plots, electrochemical impedance spectra (EIS), and linear sweep voltammetry (LSV) were acquired on a Zennium E station (ZAHNER, Germany) in a three-electrode system consisting of a working electrode (catalyst-precoated glassy carbon electrode), counter electrode (Pt wire), and reference electrode (Ag/AgCl); the electrolyte is 0.5 M Na_2SO_4. For the LSV measurement, the above hole sacrificial agent with same concentration to photocatalytic tests was added to enhance the photoelectron signal. For the EIS measurement, the applied potential is 0.15 V [versus E^{Θ}(Ag/AgCl)]. Photocurrent signals were collected on a CHI840C electrochemical workstation (Chenhua Instrument, China) with the above standard three-electrode configuration at an applied potential of 0.23 V [versus E^{Θ}(Ag/AgCl)], where the working electrode is catalyst-precoated fluorine doped tin oxide (FTO) (coated area: 1 × 1.5 cm^2). All the working electrode was prepared as follows: 5 mg of sample was dispersed in a mixed solution of ethylene glycol (30 μL), ethanol (50 μL), and Nafion (6 μL) to form a suspension, and 8 μL of the suspension was uniformly coated on the surface of a FTO glass/glassy carbon electrode to obtain 1 × 1.5 cm^2 coating. A 300 W xenon lamp (Microsolar 300, Beijing Perfectlight, China) was used as the source of full light irradiation. The zeta potential was measured in a mixed solution of water (50 mL) and ethanol (50 mL) using a Zetasizer Nano ZS90 (UK).

Theoretical Methods. DFT-based first-principles calculations were performed using the projected augmented wave[39] method implemented in the Vienna Ab initio Simulation Package.[40,41] The Kohn−Sham one-electron states were expanded using the plane-wave basis set with a kinetic energy cutoff of 500 eV. The Perdew−Burke−Ernzerhof[42] exchange−correlation functional within the generalized gradient approximation was employed. The $MnCd_2S_3$ (100) surface was modeled by a periodic 12-layer slab repeated in 2 × 1 surface unit cell with S−Mn-termination to study the mechanistic details of surface reactions. The heterostructure model C/MCS HNRs was created by placing the graphene layer with a $\sqrt{3}$ × 4 supercell (8.52 × 9.84 $Å^2$) onto a 12-layer-thick 2 × 1 $MnCd_2S_3$ (100) slab (8.27 × 9.81 $Å^2$). For the heterostructures studied in this work, we used the averaged lateral lattice constants (of the supercells) to minimize the strain on both subsystems. Two of the graphene C atoms were

https://doi.org/10.1021/acscatal.4c06476
ACS Catal. 2025, 15, 2315−2327

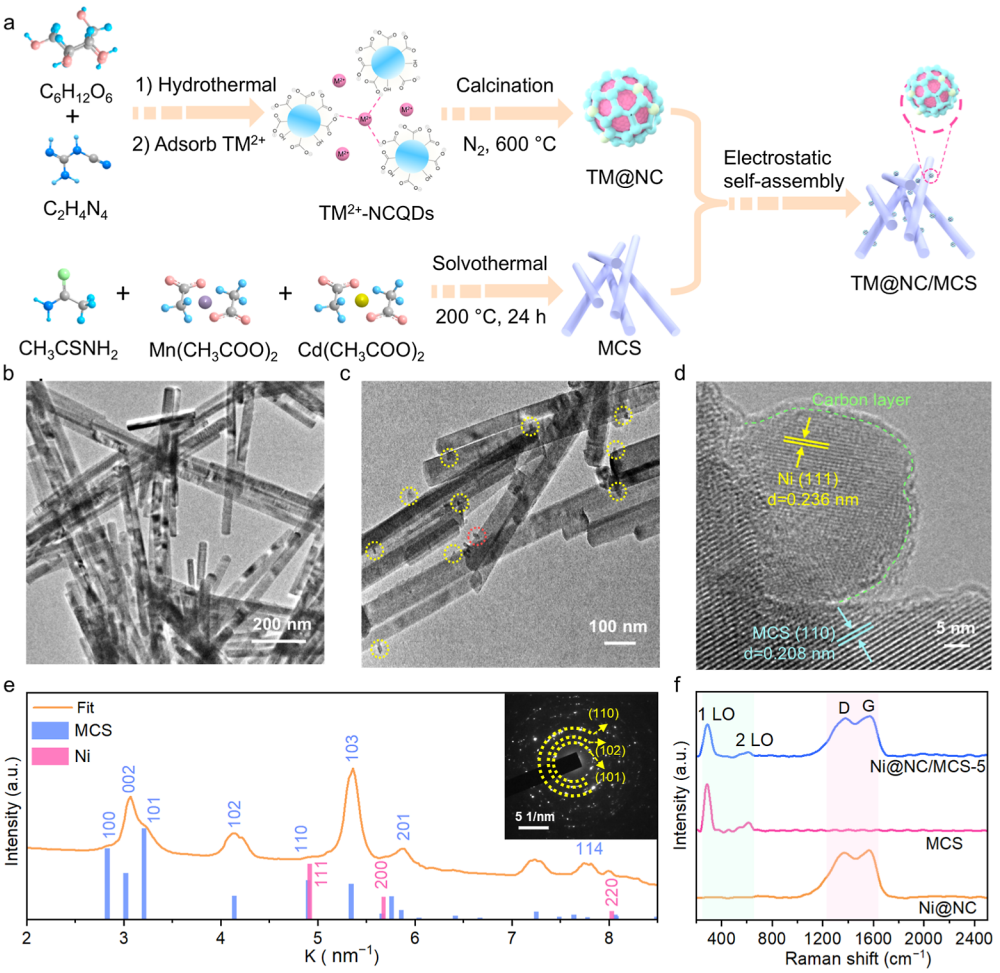

Figure 2. (a) Schematic illustration of the synthetic process of the Ni@NC/MCS HNRs. (b,c) TEM and (d) HRTEM images of the Ni@NC/MCS-5 HNRs. (e) Averaged position and intensity of diffraction rings of the SAED pattern (inset) of the Ni@NC/MCS-5 HNRs. (f) Raman spectra of the Ni@NC/MCS-5 HNRs, bare MCS NRs, and Ni@NC NPs (λ_{ex} = 532 nm).

substituted with two N atoms to model the NC/MCS HNRs. We considered the Ni_6 cluster adsorbed onto the NC/MCS HNRs surface to model the Ni@NC/MCS HNRs interface. The Brillouin-zone integration was carried out using the Monkhorst–Pack[43] sampling method with a density of 4 × 3 × 1 for the geometry optimizations. A sufficiently large vacuum region of 20 Å was used for all of the systems to ensure the periodic images were well separated. During the geometry optimizations, all the atoms were allowed to relax until the maximum magnitude of the force acting on the atoms was smaller than 0.03 eV $Å^{-1}$, and the total energy convergence criterion was set to 1×10^{-4} eV.

Under the standard conditions, the overall HER pathway includes two steps: first, adsorption of H on the catalytic site (*) from the initial state ($H^+ + e^- + *$), and second, release of the product hydrogen ($1/2H_2$). Therefore, the Gibbs free energy of the adsorption of the H* on a catalyst (ΔG_{H^*}) is the key descriptor of the HER activity of the catalyst and was obtained by[44]

$$\Delta G_{H^*} = \Delta E_H + \Delta ZPE - T\Delta S \quad (2)$$

where ΔE_H, ΔZPE, and ΔS are the adsorption energy, zero-point energy change, and entropy change of H adsorption, respectively.

$\Delta\rho$ was obtained using the following equation: $\Delta\rho = \rho\,(AB) - \rho\,(A) - \rho\,(B)$, where $\rho\,(AB)$, $\rho\,(A)$, and $\rho\,(B)$ are the total charge density of the A = MCS HNRs and B = C, NC, Ni_6, and NC, respectively.

RESULTS AND DISCUSSION

Synthetic Route and Microstructure Characterizations. The TM@NC/MCS HNRs were prepared using a modified three-step method,[10] as shown in Figure 2a. First, NCQDs were synthesized via a hydrothermal reaction of $C_6H_{12}O_6$ and $C_2H_4N_4$ at 200 °C for 6 h. TM ions (TM^{2+} = Co^{2+}, Ni^{2+}, and Cu^{2+}) are respectively adsorbed onto the surfaces of as-prepared NCQDs, forming TM^{2+}-modified NCQD precursors, which were annealed in an N_2 atmosphere at 600 °C for 2 h to obtain different TM@NC NPs. Second, the bare MCS NRs were synthesized by a solvothermal reaction of $Mn(CH_3COO)_2{\cdot}4H_2O$, $Cd(CH_3COO)_2{\cdot}2H_2O$, and CH_3CSNH_2 in a mixed solvent of deionized water and ethylenediamine at 200 °C for 24 h. Finally, the TM@NC/MCS HNRs were prepared by electrostatic attraction between TM@NC NPs and MCS NRs with oppositive surface charge in the mixed solvent of absolute ethanol and water, as evidenced by their zeta potentials in Figure S6. Next, the Ni@NC/MCS-5 HNRs were taken as a representative case for detailed microstructure analysis.

https://doi.org/10.1021/acscatal.4c06476
ACS Catal. 2025, 15, 2315–2327

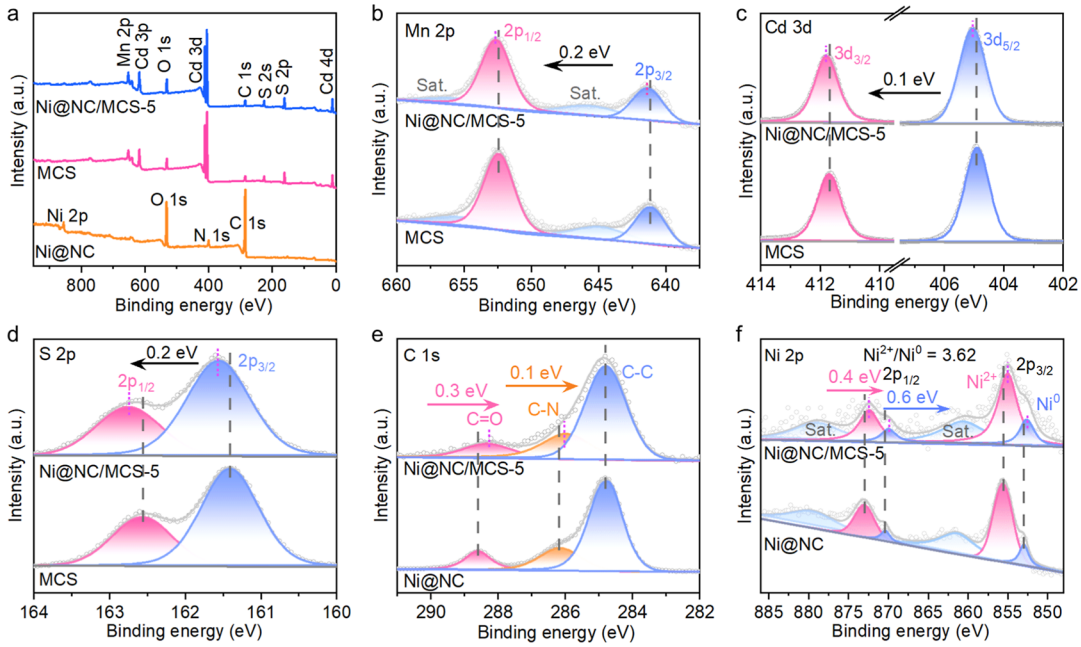

Figure 3. XPS spectra of the bare MCS NRs, Ni@NC NPs, and Ni@NC/MCS-5 HNRs: (a) survey, (b) Mn 2p, (c) Cd 3d, (d) S 2p, (e) C 1s, and (f) Ni 2p.

Figure S7a−c shows the SEM images of the bare MCS NRs, Ni@NC NPs, and Ni@NC/MCS-5 HNRs. Bare MCS NRs have a straight rod-like structure with an average length and diameter of 1.01 μm and 37.8 nm (Figure S7d,e), respectively, corresponding to an aspect ratio of 26.7 in accordance with the NR structure featuring an aspect ratio of <30.[45] The XRD analysis shows that MCS NRs have a hexagonal close-packed (hcp) structure (Figure S8). Bare Ni@NC NPs present a spherical morphology with an average diameter of 31.9 nm (Figure S7b,f), and their XRD pattern reveals the presence of face-centered cubic (fcc) metal Ni (Figure S8). For Ni@NC/MCS-5 HNRs, the supported Ni@NC NPs were not clearly observed from the SEM image and XRD pattern (Figures S7c and S8), due to low content and small size.

Figure 2b displays the TEM image of the Ni@NC/MCS-5 HNRs, confirming the straight NR structure. The high-magnification TEM image reveals the presence of ultrasmall Ni@NC NPs anchored on MCS NRs, as labeled by yellow and red dashed circles (Figure 2c). The HRTEM image obtained from the red dashed circle in Figure 2c shows close contact between Ni@NC NPs and MCS NRs, where two sets of lattice fringes are separated by the interface. The one with a *d*-value of 0.236 nm corresponds to the (111) faces of fcc-Ni, and the other one with a *d*-value of 0.208 nm corresponds to the (110) faces of hcp-MCS. Besides, the Ni@NC NPs have an amorphous shell, as separated from the crystalline region by the green dashed line (Figure 2d), indicating that the Ni NPs are coated by an ultrathin NC layer. The SAED pattern depicts a set of nonuniform and concentric rings (the inset of Figure 2e), indicating a polycrystalline structure with a certain preferential orientation for some specific crystal faces, which is caused by the rod-like structure. The fine diffraction profile further verifies that all of the diffraction signals almost result from hcp-MCS for the Ni@NC/MCS-5 HNRs without any detected impurity phases (Figure 2e). No obvious diffraction signals were indexed to the Ni@NC NPs because of their low loading amount.

The presence and microstructural characteristics of the NC layers were revealed by comparing the Raman spectra of bare MCS NRs and Ni@NC NPs, and Ni@NC/MCS-5 HNRs. As shown in Figure 2f, bare MCS NRs present two Raman bands at 288 and 613 cm^{-1}, corresponding to the stretching and bending vibration of 1 LO and 2 LO modes of MCS NRs.[46−48] Bare Ni@NC NPs display two adjacent Raman bands at 1375 and 1573 cm^{-1} indexed to D and G bands resulting from sp^2 and sp^3 hybridization of C atoms, respectively.[49−51] The intensity ratio of D and G band is 1.1, reflecting abundant defects within the NC layer,[52] which can provide an enormous number of coordination-unsaturated atoms acting as catalytically active sites.[53,54] In addition, the coexistence of Raman bands of bare MCS and Ni@NC in the Ni@NC/MCS-5 HNRs also supports the successful assembly of Ni@NC NPs on MCS NRs.

The elemental composition and chemical state were further revealed by XPS. As shown in Figures 3a and S9a, the survey XPS spectra show no impurity elements contained in all three samples except adventitious carbon (284.8 eV) and surface-adsorbed oxygen-containing species (mainly adsorbed water). For the bare MCS NRs, the Mn 2p high-resolution spectrum was fitted into a set of profiles composed of two XPS peaks at 652.4 and 641.1 eV and two satellite peaks, revealing the presence of Mn^{2+} species (Figure 3b).[55,56] The Cd 3d spectrum shows two symmetry peaks at 411.6 and 404.9 eV of Cd^{2+} species (Figure 3c).[36,57] The S 2p spectrum was deconvoluted into two XPS peaks of S^{2-} species at 162.6 and 161.4 eV (Figure 3d).[58] For the bare Ni@NC NPs, the C 1s spectrum presents three peaks at 288.6, 286.0, and 284.8 eV, corresponding to carbonates, C−N/C−O, and C−C species, respectively (Figure 3e).[59] The N chemical state includes a trace of N−O species at 404.0 eV, a certain amount of graphitic carbon ($N-C_3$) at 401.0 eV, and abundant pyridinic C−N−C at 399.0 eV (Figure S9b).[10,60,61] The Ni 2p spectrum was well fitted into two doublets except for two satellite peaks, the one at 873.0 and 855.6 eV corresponds to Ni^{2+} species, and

https://doi.org/10.1021/acscatal.4c06476
ACS Catal. 2025, 15, 2315−2327

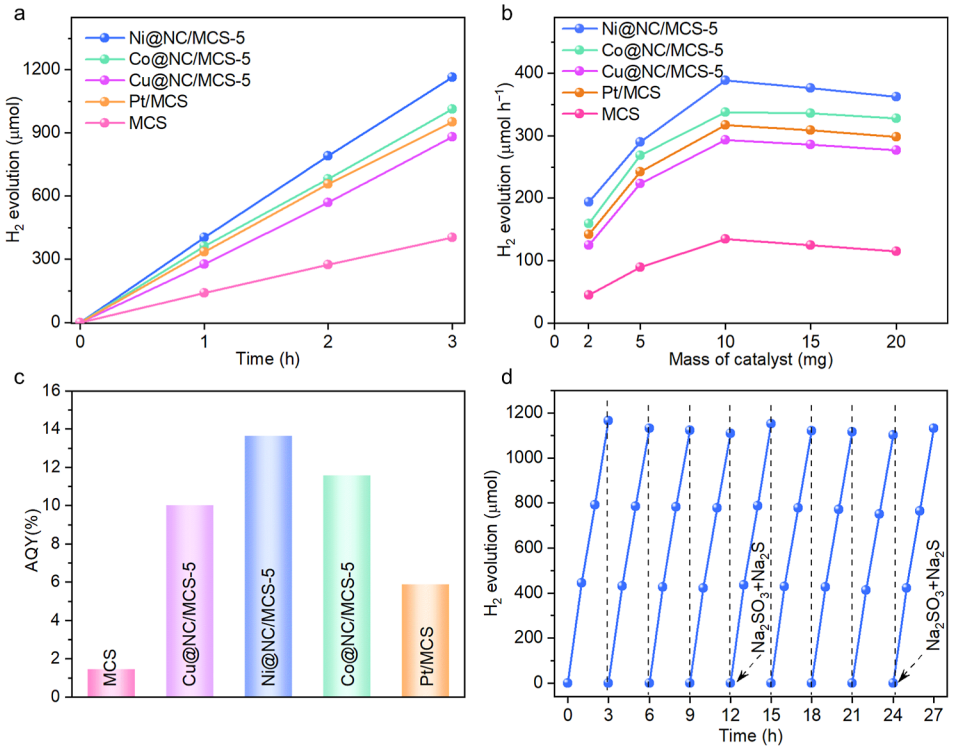

Figure 4. (a) Time courses of photocatalytic H_2 evolution. (b) H_2 evolution rate as a function of photocatalyst mass. (c) AQY under monochromatic light (λ = 400 nm) irradiation. (d) Cyclic tests of H_2 evolution over the Ni@NC/MCS-5 HNRs. (10 mg samples, irradiation intensity of full and monochromatic light: 2472.8 and 663.2 W m^{-2}, respectively.)

that at 870.4 and 853.0 eV reveals the presence of Ni^0 species (Figure 3f).[62,63] The formation of Ni^{2+} species is attributed to part oxidation of Ni NPs.[64]

Comparisons of high-resolution XPS spectra reveal electronic interactions in the Ni@NC/MCS HNRs. For the Ni@NC/MCS-5 HNRs with respect to bare Ni@NC NPs, all the Mn 2p, Cd 3d, and S 2p spectra shift toward higher binding energy (Figure 3b–d), while the C 1s and Ni 2p spectra move toward lower binding energy (Figure 3e,f). Note that the shift direction of the N 1s spectrum is not consistent with those of C 1s and Ni 2p (Figure S9b), which might be disturbed by the adjacent Cd $3d_{5/2}$ peak. Taken together with the relatively low content of N elements in the Ni@NC/MCS HNRs, the shift magnitude of the N 1s spectrum may fall into an error range and was not thus considered. Collectively, the above results demonstrate evident interfacial interaction between Ni@NC and MCS in Ni@NC/MCS HNRs, which supports the DFT result.

The microstructures of Co@NC/MCS and Cu@NC/MCS HNRs are presented in Figure S10. Similarly, the MCS NR-supported Co@NC and Cu@NC NPs were not observed clearly due to their small size and low loading amount (Figure S10a,b). However, both of XRD and Raman analyses reveal the coexistence of MCS NRs and Co@NC or Cu@NC NPs (Figure S10c–f). As the TM salts were further substituted by the adjacent elements of Fe and Zn, i.e., Fe(III) and Zn(II) nitrates, in the preparation process of TM@NC NPs, the corresponding TM@NC NPs were not formed. The metal oxides/nitrides were obtained instead, as shown in Figure S11a–d. It means that the present synthetic strategy for TM@NC NPs only displays a certain universality for specific TMs (Co, Ni, and Cu).

Photocatalytic HER Performance. The photocatalytic HER performance was assessed using a liquid–solid (water-TM@NC/MCS HNRs) mode with Na_2SO_3 and Na_2S as hole sacrificial agents under full light irradiation. As shown in Figure 4a, bare MCS NRs can catalytically reduce water to H_2, showing an H_2 evolution rate of 134.3 μmol h^{-1}. After different cocatalysts are loaded, the photocatalytic activity is enhanced at different levels. In particular, the H_2 evolution rate of the Ni@NC/MCS-5 HNRs reaches 388.4 μmol h^{-1}, which is 2.9 times that of bare MCS NRs and also outperforms those of Co@NC/MCS-5, Cu@NC/MCS-5, and even Pt NP-loaded MCS (Pt/MCS) HNRs. Note that the loading amount of these cocatalysts (Ni@NC and Pt NPs) and the Ni content in Ni@NC have been optimized, as shown in Figure S12a–d. Since the H_2 evolution rate is not directly proportional to the mass of photocatalysts,[65−67] the mass of photocatalysts was optimized in terms of the highest H_2 evolution rate for different photocatalysts, as shown in Figure 4b. It was found that the H_2 evolution rate gradually increased from 2 to 10 mg and slightly declined from 10 to 20 mg. The slight decline in H_2 evolution rate with excess photocatalysts results from the agglomeration of photocatalysts that inhibit the light penetration.[68−70] It means that 10 mg is sufficient to maximize the light utilization for all the photocatalysts under the present test conditions, corresponding to the optimal mass. A series of control experiments show hardly any H_2 evolution in the reaction system without the addition of catalysts, illumination, or sacrificial agent (Figure S13), verifying Ni@NC/MCS HNR-catalyzed water reduction under normal conditions. AQY was measured under different monochromatic light irradiations for all of the TM@NC/MCS-5 HNRs, as shown in Figure S14. As a representative case, the detailed parameters for determining the AQY of the Ni@NC/MCS-5 HNRs are

https://doi.org/10.1021/acscatal.4c06476
ACS Catal. 2025, 15, 2315−2327

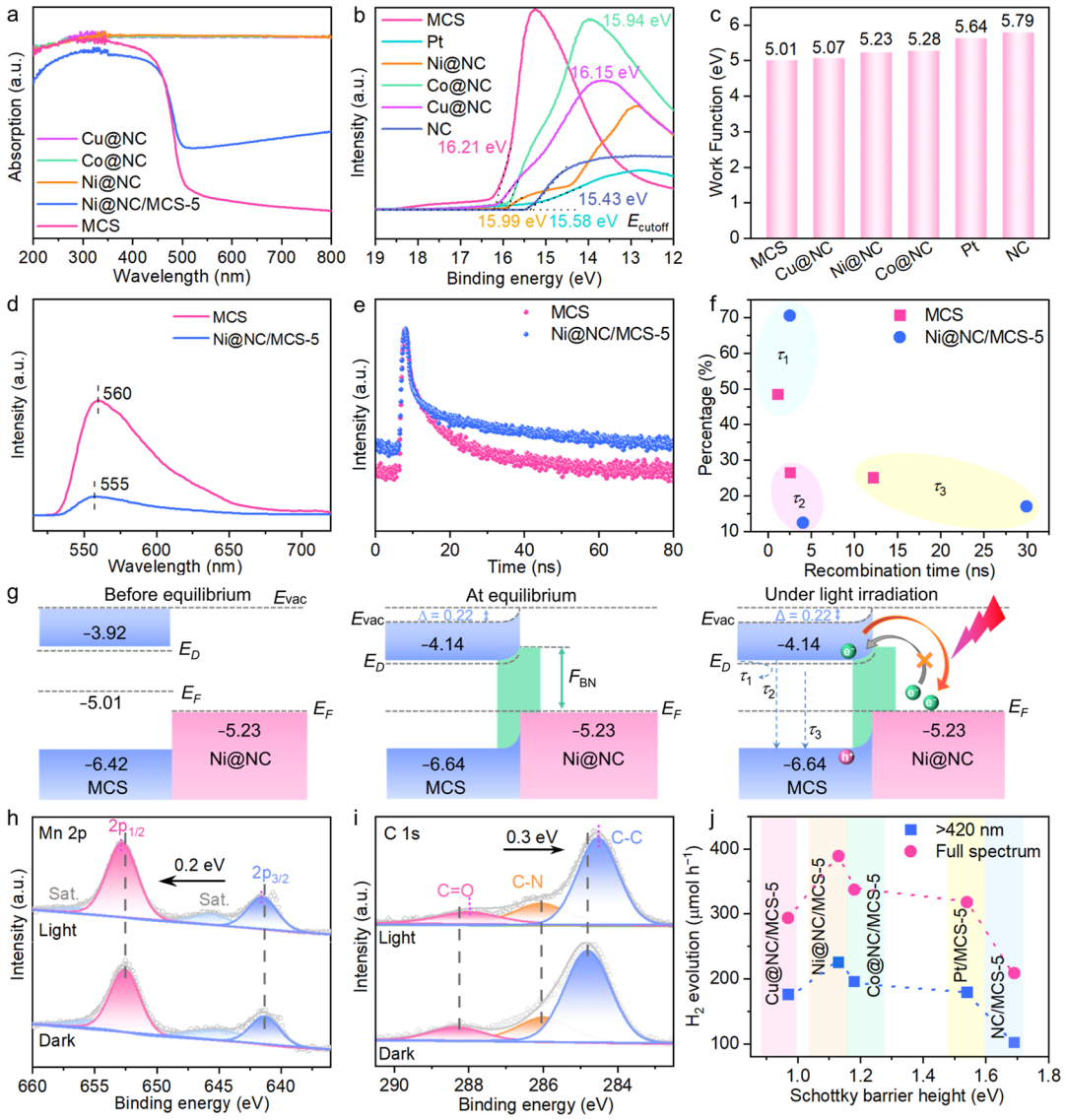

Figure 5. (a) UV−vis DRS, (b) UPS spectra, and (c) Φ of different samples. (d) PL spectra, (e) TRPL spectra, and (f) corresponding decay components and percentage of the bare MCS NRs and Ni@NC/MCS-5 HNRs. (g) Illustration of band structures of the bare MCS NRs and Ni@NC NPs, and charge transfer pathway in the Ni@NC/MCS HNRs under irradiation. E_{vac}, vacuum level; E_D, defect level; F_{BN} presents Schottky barrier height. The red arrows indicate electron transfer direction. Δ refers to the contact potential difference at the interface. All the energy levels are versus RHE (V). (h) Mn 2p and (i) C 1s high-resolution XPS spectra of the Ni@NC/MCS-5 HNRs with (without) irradiation. (j) Relationship between photocatalytic HER activity and Schottky barrier height for different samples (10 mg) under visible-light (420 nm < λ < 780 nm with an intensity: 1253.6 W m^{-2}) and full light irradiation, respectively.

presented in Table S1. The AQY reduces with the increase of irradiation wavelength for all the HNRs. For further comparison of the photocatalytic HER activity, the AQY of bare MCS NRs and Pt/MCS HNRs were determined under the irradiation of λ = 400 nm, as shown in Figure 4c. The AQY of the Ni@NC/MCS-5 HNRs is 13.6%, which is 9.7 times that of MCS and also higher than those of other TM@NC/MCS-5 and even Pt/MCS HNRs.

In addition, the stability of photocatalytic HER over Ni@NC/MCS HNRs was assessed by a consecutive cyclic test containing 9 runs with each run of 3 h. As shown in Figure 4d, the H_2 evolution rate slightly decreased after four runs with a total of 12 h due to the consumption of the sacrificial agent. As the concentration of the sacrificial agent was replenished to the initial value, the H_2 evolution rate immediately recovered to the highest value, demonstrating good photocatalytic HER stability of Ni@NC/MCS HNRs. Furthermore, the microstructure characterizations on the spent catalysts, including XRD, SEM, and XPS (Figure S15a−f), verify the structural stability of Ni@NC/MCS HNRs.

Band Structure and Carrier Separation Kinetics. The effect of the specific surface area was examined prior to band structure analysis to address the enhanced photocatalytic activity. As shown in Figure S16a,b, the loading of Ni@NC NPs exerts little influence on the average pore size distribution, while the specific surface area increases by 0.7 times. Since the decoration of Ni@NC NPs remarkably promotes carrier separation efficiency, the increment of specific surface area is also considered to contribute to the photocatalytic activity.[65] Even so, the increment is obviously inferior to that of the photocatalytic activity, indicating that the surface area is not the main factor governing photocatalytic activity.

https://doi.org/10.1021/acscatal.4c06476
ACS Catal. 2025, 15, 2315−2327

The band structures of TM@NC/MCS HNRs were investigated by a combined analysis of UV−vis DRS, Mott−Schottky plots, and UPS. The UV−vis DRS of bare MCS NRs shows an absorption edge of 521 nm to the entire region (Figure 5a). The corresponding Tauc plot was fitted by the equation of $\alpha h\nu \propto (h\nu - E_g)^2$, where α, h, ν, and E_g are absorbance, Planck constant, light frequency, and the bandgap value of the semiconductor, respectively (Figure S17a), indicating direct-allowed electronic transitions and an E_g value of 2.50 eV. By contrast, all bare TM@NC NPs have very close absorption profiles to the full light spectrum. Compared with bare MCS NRs, the loading of TM@NC NPs greatly increases the absorbance in the visible-light region. The Mott−Schottky plots of bare MCS NRs at different frequencies are linearly fitted to intercept with the horizontal axis (Figure S17b), and the flat band potential was thus determined at −0.52 V (vs RHE). The UPS spectra of bare MCS NRs, different bare TM@NC NPs, Pt NPs, and bare NC are shown in Figure 5b; all the Φ was determined from the cutoff edge according to the relations in Figure S18.[71] As shown in Figure 5c, Φ is the largest for bare NC followed by Pt NPs and is the smallest for MCS NRs, and the Φ of all of the TM@NC NPs falls between those of MCS NRs and Pt NPs.

PL and TRPL were used to probe the defect state and carrier decay kinetics.[72−74] As shown in Figure 5d, the loading of Ni@NC NPs reduces markedly the PL emission of MCS NRs due to electrons transfer from MCS NRs to Ni@NC NPs.[75] Note that the emission wavelength is focused around 560 nm for bare MCS NRs, corresponding to a photon energy of 2.2 eV, lower by 0.3 eV than the E_g (2.50 eV). The defect level is thus concluded to be located at ∼0.3 eV below CBM for MCS NRs.[76,77] Furthermore, the TRPL spectra were well fitted with a three-exponential decay model to study the photogenerated carrier lifetime and migration paths, as shown in Figure 5e,f. According to the previous reports,[74,78−82] the fast decay component (τ_1) represents defect-assisted trapping, that is, electrons relaxing from CBM to defect levels.[82] Provided that the delay time of internal separated charge (i.e., free electrons and holes) is at least 1 order of magnitude longer than that of unsegregated electron−hole pairs (excitonic states),[78,81] the decay components (τ_2 and τ_3) represent the delay lifetime of excitonic states and internal separated charge, respectively (Figure 5f). Comparisons of decay components between bare MCS NRs and Ni@NC/MCS HNRs reveal that loading Ni@NC NPs slightly increases the τ_1 value while markedly promoting its proportion, indicating enhanced defect-state trapping, which may result from metal-induced gap state in the MCS NRs.[25,83] Similarly, the presence of Ni@NC NPs exerts little influence on the τ_2 value while significantly reducing its share, suggesting markedly reduced recombination possibility of excitonic states. Moreover, the increased τ_3 value indicates a longer lifetime of free carriers, while the relatively low proportion of τ_3 illustrates that a large number of free electrons are transferred from the MCS to Ni@NC within Ni@NC/MCS HNRs.

As shown in Figure 5g, bare MCS NRs have a higher E_F than bare Ni@NC NPs before contact. Upon close contact, electrons transfer from the MCS side to Ni@NC side in their interface until Fermi equilibrium, resulting in the formation of a space charge region and built-in electric field pointing from MCS to Ni@NC. Meanwhile, an upward band bending is caused at the MCS side to stop electrons' further flow, and a Schottky barrier is formed between the two components to prevent backflow. Under irradiation, a lot of photoelectrons are excited from valence bands to conduction bands of the MCS NRs, where energetic electrons can jump the interfacial band bending and flow into the Ni@NC NPs for reduction half-reactions, leaving holes relaxing to the valence band maximum of MCS NRs for oxidation half-reactions. In situ-irradiated XPS spectra proved the proposed charge transfer pathway in addition to unchanged elemental composition (Figure S19a). Under the irradiation of a full light spectrum, the Mn 2p, Cd 3d, and S 2p XPS peaks shift toward a higher binding energy (Figures 5h and S19b,c), while the C 1s XPS peaks move toward a lower binding energy (Figure 5i), and the Ni 2p XPS peaks remain roughly unchanged (Figure S19d), confirming photoelectrons flow from MCS to Ni@NC within Ni@NC/MCS HNRs. The correlation of photocatalytic activity with the Schottky barrier height (F_{BN}) is shown in Figure 5j. As the F_{BN} increases, the H_2 evolution rate presents a volcano-like evolution profile under the irradiation of the full light spectrum, indicating moderate F_{BN} is necessary for obtaining the highest photocatalytic activity. After the deduction of high-energy ultraviolet light from the full spectrum, which reduces the percentage of energetic electrons, the photocatalytic activity trend remains unchanged, verifying the F_{BN}-dependent photocatalytic activity. This can be rationalized by the following analysis. Larger F_{BN} decreases the share of photoelectrons jumping interfacial band bending and thus reduces carrier separation efficiency. However, smaller F_{BN} easily causes electron counterflow from TM@NC NPs to MCS NRs, leading to a decline of photoelectrical efficiency. Naturally, a moderate F_{BN} is necessary to achieve the highest separation efficiency.

The F_{BN}-dependent photocatalytic activity is supported by a series of theoretical and experimental evidence on the electrocatalytic activity of cocatalysts and physicochemical properties of the cocatalyst/MCS heterojunctions. First, although there is a certain difference in electronic structure among Co@NC, Ni@NC, and Cu@NC NPs, the electronegativity is very close for the three metals, that is, 1.88, 1.91, and 1.90 for Co, Ni, and Cu, respectively. Thus, all the TM@NC may possess similar intrinsic catalytic activity toward HER. As expected, the LSV spectra show that they have very close electrocatalytic HER activity (onset potential and current density at the same applied potential), which are inferior to that of the Pt NPs (Figure S20a). In addition, the Pt/MCS model has the smallest adsorption energy to H* species (Figure 1h) and features the fastest H_2 evolution rate from the perspective of surface reaction in theory. These results are not consistent with the trend of photocatalytic activity of TM@NC/MCS and Pt/MCS, indicating that the catalytic activity of cocatalysts is not the key factor governing photocatalytic activity. Although the electrocatalytic activity is significantly reduced upon hybrid with MCS NRs (Figure S20b) due to the low conductivity of MCS, the electrocatalytic activity of Ni@NC/MCS and Co@NC/MCS HNRs becomes better than that of the Pt/MCS HNRs, due to higher interfacial charge transfer efficiency.[84] In particular, the onset potential reduces and current density at the same potential increases for all the hybrids under light irradiation, indicating the boosted HER by photoelectrons. Furthermore, the interfacial charge transfer efficiency was investigated by EIS. All the TM@NC/MCS and Pt/MCS HNRs display a smaller Nernst semicircle than bare MCS NRs (Figure S21), indicating reduced charge-transfer resistance. The fitting of the EIS spectra by the equivalent

https://doi.org/10.1021/acscatal.4c06476
ACS Catal. 2025, 15, 2315−2327

circuit (inset of Figure S21) reveals that interfacial charge transfer resistance (R_{ct}) is the lowest for Ni@NC/MCS HNRs (Table S2), implying the fastest electron transfer within Ni@NC/MCS HNRs and between it and the electrolyte,[85] which supports the LSV results. Second, photocurrent response under chopped irradiation provides direct evidence of the separation efficiency of photogenerated carriers within these Schottky junctions. As shown in Figure S22a, all the Schottky junctions show silent photocurrent signal in the dark, which rapidly increases to a platform at a different level upon irradiation and declines fast to the initial value after the light is off during four-run cyclic tests. As the Schottky barrier height increases, the photocurrent density also presents a volcano-like evolution trend (Figure S22b), which is consistent with the order of their photocatalytic activity. Additionally, the Pt/MCS HNRs show lower current density and photocatalytic activity than both Ni@NC/MCS and Co@NC/MCS HNRs under irradiation, due to exorbitant Schottky barrier height. These results verify the best separation of photogenerated carriers by moderate Schottky barrier height.

As mentioned above, the Schottky barrier height at the TM@NC/semiconductor interfaces can be modulated by varying the metal element. However, it is improper to change the type of host semiconductor for tuning Schottky barrier height since different semiconductors have essential differences in the ability of light absorption and carrier transport. Alternatively, for the same metal-based hybrid such as Ni@NC/MCS, it is possible to refine the Schottky barrier height by changing the percentage of the oxidation state of Ni. As shown in Figure S23a and b, the Ni^0@NC and Ni^{2+}@NC NPs have lower and higher percentages of Ni^{2+} oxidation sate than the Ni@NC NPs. The Φ was determined to be 5.29 and 5.04 eV for Ni^0@NC and Ni^{2+}@NC, respectively, by UPS analysis (Figure S23c,d), while the Φ of Ni@NC falls between them. Figure S23e shows the photocatalytic H_2 evolution rate over the three control samples. As can be seen, the photocatalytic activity is slightly altered with the increase of Ni^{2+} oxidation state. Considering catalytical sites located at the NC layer and the percentage of Ni^{2+} oxidation state as the only variable, the fluctuation of photocatalytic activity should result from the change of Schottky barrier height caused by the different percentage of Ni^{2+} oxidation state (Figure S23f). This result demonstrates that moderate Schottky barrier height is necessary to optimize photocatalytic activity of the same metal-based hybrids by adjusting the percentage of the oxidation state in the metal component. Taken together with that in Figure 5j, as Schottky barrier height increases in the range of 0.9−1.7, the photocatalytic HER activity gradually increases, reaching the maximum on the Ni@NC/MCS HNRs with a Schottky barrier height of 1.13 eV, and then declines, presenting a volcano-like evolution trend.

In addition to providing abundant catalytic sites, the NC layer also plays a vital role in the formation of TM NPs and in protecting it from overoxidation. As shown in Figures 3f and S23a,b, the zerovalent Ni is always contained in the Ni^0@NC, Ni@NC, and Ni^{2+}@NC NPs, due to the presence of NC. In contrast, the absence of NCQDs in the preparation process of Ni@NC results in the formation of NiO NPs (Figure S24a), while the NiO/MCS-5 HNRs show significantly lower photocatalytic HER activity than Ni@NC/MCS HNRs (Figure S24b). Since NiO is a wide-bandgap semiconductor, the charge transfer mechanism is obviously different from that of the Schottky junctions,[86] which is not the focus of this work. Besides, the photocatalytic activity is further reduced for NC/MCS HNRs with respect to Ni@NC/MCS HNRs, indicating that Ni@NC is a better cocatalyst than NiO and NC. The low photoactivity of NC/MCS results from the largest F_{BN} at the heterogeneous interface, which only allows less electrons to transfer from MCS to NC under irradiation. In addition, the decoration of Ni@NC NPs reduces the contact angle between catalysts and water (Figure S25a,b) and enhances the adsorption to H_2O molecules on Ni@NC/MCS HNRs with respect to bare MCS NRs.

CONCLUSIONS

A cocatalyst synthetic strategy with non-noble TMs and NC has been developed to boost the photocatalytic HER activity of MCS NRs. The TM@NC NPs with large Φ enhance electron trapping from MCS NRs under irradiation. Meanwhile, the Schottky barrier height at the interface of TM@NC NPs and MCS NRs is efficient to adjust the transfer of electrons from MCS to TM@NC. Among the examined metals, the Ni@NC NPs exhibit an optimized Schottky barrier height, which effectively facilitates electron transfer and suppresses backflow, leading to the highest carrier separation efficiency. The metal NPs refine the electronic structure of the NC layer and endow the TM@NC/MCS HNRs with moderate adsorption capability to H*. Moreover, the NC layer, in turn, not only protects the metal NPs from overoxidation but also provides abundant catalytically active sites for HER. As a result, all the TM@NC/MCS HNRs exhibit significantly enhanced photocatalytic HER activity compared with bare MCS NRs, and the Ni@NC/MCS HNRs' performance is even more superior to the performance of optimized Pt/MCS HNRs.

ASSOCIATED CONTENT

Supporting Information

The Supporting Information is available free of charge at https://pubs.acs.org/doi/10.1021/acscatal.4c06476.

Optical photographs, equipment and method, zeta potential, AQY, SEM images, XRD patterns, Raman spectra, XPS spectra, control experiments, nitrogen adsorption−desorption isotherms, Tauc plots, Mott−Schottky plots, in situ-irradiated XPS spectra, (photo)-electrochemical spectra, energy level information for UPS analysis, contact angles, and DOS (PDF)

AUTHOR INFORMATION

Corresponding Authors

Changfa Guo − *Key Laboratory of the Ministry of Education for Advanced Catalysis Materials, Department of Chemistry, Zhejiang Normal University, Jinhua 321004, China;* orcid.org/0000-0002-0432-8121; Email: changfa.guo@zjnu.edu.cn

Wentao Wang − *Guizhou Provincial Key Laboratory of Computational Nano-Material Science, Guizhou Education University, Guiyang 550018, China;* orcid.org/0000-0003-4308-3515; Email: wtwang@gznc.edu.cn

Yong Hu − *College of Chemistry and Materials Engineering, Zhejiang A&F University, Hangzhou 311300, China;* orcid.org/0000-0003-3777-167X; Email: yonghu@zafu.edu.cn, yonghu@zjnu.edu.cn

https://doi.org/10.1021/acscatal.4c06476
ACS Catal. 2025, 15, 2315−2327

Authors

Yufeng Li − *Key Laboratory of the Ministry of Education for Advanced Catalysis Materials, Department of Chemistry, Zhejiang Normal University, Jinhua 321004, China*

Songqing Zhang − *Key Laboratory of the Ministry of Education for Advanced Catalysis Materials, Department of Chemistry, Zhejiang Normal University, Jinhua 321004, China*

Chunmei He − *Key Laboratory of the Ministry of Education for Advanced Catalysis Materials, Department of Chemistry, Zhejiang Normal University, Jinhua 321004, China*

Hongxia Yao − *Key Laboratory of the Ministry of Education for Advanced Catalysis Materials, Department of Chemistry, Zhejiang Normal University, Jinhua 321004, China*

Complete contact information is available at: https://pubs.acs.org/10.1021/acscatal.4c06476

Author Contributions

‖Y.L. and S.Z. contributed equally to this work.

Notes

The authors declare no competing financial interest.

■ ACKNOWLEDGMENTS

This work is financially supported by the National Natural Science Foundation of China (22272150, 22472155, 22102145, 52262031), the Major Program of Zhejiang Provincial Natural Science Foundation of China (LD22B030002), Zhejiang Provincial Ten Thousand Talent Program (2021R51009), the Zhejiang Provincial Natural Science Foundation of China (LY22B030012), and Guizhou provincial People's Government (Department of Education) Scholarship for Overseas Studies. The work is carried out at Shanxi Supercomputing Center of China, and the calculations are performed on TianHe-2. This research is also supported by the advanced computing resources provided by the Supercomputing Center of the University of Science and Technology of China.

■ REFERENCES

(1) Chen, X.; Shen, S.; Guo, L.; Mao, S. S. Semiconductor-based photocatalytic hydrogen generation. *Chem. Rev.* **2010**, *110* (11), 6503−6570.

(2) Kudo, A.; Miseki, Y. Heterogeneous photocatalyst materials for water splitting. *Chem. Soc. Rev.* **2009**, *38* (1), 253−278.

(3) Zhou, P.; Navid, I. A.; Ma, Y.; Xiao, Y.; Wang, P.; Ye, Z.; Zhou, B.; Sun, K.; Mi, Z. Solar-to-hydrogen efficiency of more than 9% in photocatalytic water splitting. *Nature* **2023**, *613* (7942), 66−70.

(4) Tang, J.; Durrant, J. R.; Klug, D. R. Mechanism of photocatalytic water splitting in TiO_2. Reaction of water with photoholes, importance of charge carrier dynamics, and evidence for four-hole chemistry. *J. Am. Chem. Soc.* **2008**, *130* (42), 13885−13891.

(5) Maeda, K.; Teramura, K.; Domen, K. Effect of post-calcination on photocatalytic activity of $(Ga_{1-x}Zn_x)(N_{1-x}O_x)$ solid solution for overall water splitting under visible light. *J. Catal.* **2008**, *254* (2), 198−204.

(6) Lide, D. R. *CRC Handbook of Chemistry and Physics*, 85th ed.; CRC: Boca Raton; FL, 2004.

(7) Ran, J.; Zhang, J.; Yu, J.; Jaroniec, M.; Qiao, S. Z. Earth-abundant cocatalysts for semiconductor-based photocatalytic water splitting. *Chem. Soc. Rev.* **2014**, *43* (22), 7787−7812.

(8) Wang, S.; Wang, Y.; Zhang, S.; Zang, S.; Lou, X. Supporting ultrathin $ZnIn_2S_4$ nanosheets on Co/N-doped graphitic carbon nanocages for efficient photocatalytic H_2 generation. *Adv. Mater.* **2019**, *31* (41), 1903404.

(9) Zhang, K.; Ran, J.; Zhu, B.; Ju, H.; Yu, J.; Song, L.; Qiao, S. Z. Nanoconfined nickel@carbon core−shell cocatalyst promoting highly efficient visible-light photocatalytic H_2 production. *Small* **2018**, *14* (38), 1801705.

(10) Meng, X.; Zhang, C.; Dong, C.; Sun, W.; Ji, D.; Ding, Y. Carbon quantum dots assisted strategy to synthesize Co@NC for boosting photocatalytic hydrogen evolution performance of CdS. *Chem. Eng. J.* **2020**, *389*, 124432.

(11) Tan, M.; Huang, C.; Yu, C.; Li, C.; Yin, R.; Liu, C.; Dong, W.; Meng, H.; Su, Y.; Qiao, L.; Gao, L.; Lu, Q.; Bai, Y. Unexpected high-performance photocatalytic hydrogen evolution in Co@NCNT@$ZnIn_2S_4$ triggered by directional charge separation and transfer. *Small* **2022**, *18* (49), 2205266.

(12) Li, X.; Song, S.; Gao, Y.; Ge, L.; Song, W.; Ma, T.; Liu, J. Identification of the charge transfer channel in cobalt encapsulated hollow nitrogen-doped carbon matrix@CdS heterostructure for photocatalytic hydrogen evolution. *Small* **2021**, *17* (31), 2101315.

(13) Liu, X.; Yang, X.; Cui, J.; Wu, C.; Sun, Y.; Du, X.; Chen, J.; Ye, J.; Liu, L. Ni coated with N-doped graphene Layer as active and stable H_2 evolution cocatalysts for photocatalytic overall water splitting. *ACS Catal.* **2023**, *13* (21), 14314−14323.

(14) Xu, D.; Zhang, S. N.; Chen, J. S.; Li, X. H. Design of the synergistic rectifying interfaces in Mott−Schottky catalysts. *Chem. Rev.* **2023**, *123* (1), 1−30.

(15) Liu, C.; Zhang, Y.; Wu, J.; Dai, H.; Ma, C.; Zhang, Q.; Zou, Z. Ag-Pd alloy decorated $ZnIn_2S_4$ microspheres with optimal Schottky barrier height for boosting visible-light-driven hydrogen evolution. *J. Mater. Sci. Technol.* **2022**, *114*, 81−89.

(16) Žerjav, G.; Zavašnik, J.; Kovač, J.; Pintar, A. The influence of schottky barrier height onto visible-light triggered photocatalytic activity of TiO_2 + Au composites. *Appl. Surf. Sci.* **2021**, *543*, 148799.

(17) Žerjav, G.; Roškarič, M.; Zavašnik, J.; Kovač, J.; Pintar, A. Effect of Au loading on Schottky barrier height in TiO_2 + Au plasmonic photocatalysts. *Appl. Surf. Sci.* **2022**, *579*, 152196.

(18) Wang, P.; Cai, Y.; Mo, W.; Fan, Z.; Li, Z.; Wu, L.; Zhong, S.; Bai, S. Modulating the Schottky barrier heights of plasmonic metal/semiconductor heterojunctions by graphene substrates for boosting photocatalytic water oxidation. *Appl. Surf. Sci.* **2024**, *642*, 158561.

(19) Qiao, X. Q.; Li, C.; Chen, W.; Guo, H.; Hou, D.; Sun, B.; Han, Q.; Sun, C.; Li, D. S. Optimization of Schottky barrier height and LSPR effect by dual defect induced work function changes for efficient solar-driven hydrogen production. *Chem. Eng. J.* **2024**, *490*, 151822.

(20) Lu, S.; Weng, B.; Chen, A.; Li, X.; Huang, H.; Sun, X.; Feng, W.; Lei, Y.; Qian, Q.; Yang, M. Q. Facet engineering of Pd nanocrystals for enhancing photocatalytic hydrogenation: modulation of the Schottky barrier height and enrichment of surface reactants. *ACS Appl. Mater. Interfaces* **2021**, *13* (11), 13044−13054.

(21) Miao, R.; Bao, Y.; Yang, G.; Sun, Y.; Wang, X.; Zhao, J.; Mu, H.; Li, F. Lowering Schottky barrier in MoC-based cocatalyst via heteroatoms tunning for enhanced photocatalytic hydrogen evolution. *Chem. Eng. J.* **2024**, *497*, 154909.

(22) Wang, A.; Wu, S.; Dong, J.; Wang, R.; Wang, J.; Zhang, J.; Zhong, S.; Bai, S. Interfacial facet engineering on the Schottky barrier between plasmonic Au and TiO_2 in boosting the photocatalytic CO_2 reduction under ultraviolet and visible light irradiation. *Chem. Eng. J.* **2021**, *404*, 127145.

(23) Cao, S.; Li, H.; Li, Y.; Zhu, B.; Yu, J. Dependence of exposed facet of Pd on photocatalytic H_2-production activity. *ACS Sustain. Chem. Eng.* **2018**, *6* (5), 6478−6487.

(24) Liu, Y.; Gu, X.; Qi, W.; Zhu, H.; Shan, H.; Chen, W.; Tao, P.; Song, C.; Shang, W.; Deng, T.; et al. Enhancing the photocatalytic hydrogen evolution performance of a metal/semiconductor catalyst through modulation of the Schottky barrier height by controlling the orientation of the interface. *ACS Appl. Mater. Interfaces* **2017**, *9* (14), 12494−12500.

(25) Nithya, P. M.; Devi, L. G. Effect of surface Ag metallization on the photocatalytic properties of $BaTiO_3$: surface plasmon effect and

variation in the Schottky barrier height. *Surf. Interfaces* **2019**, *15*, 205−215.
(26) Meng, Z.; Zhang, J.; Jiang, C.; Trapalis, C.; Zhang, L.; Yu, J. Dynamics of electron transfer in CdS photocatalysts decorated with various noble metals. *Small* **2024**, *20* (21), 2308952.
(27) Yang, J.; Wang, D.; Han, H.; Li, C. Roles of cocatalysts in photocatalysis and photoelectrocatalysis. *Acc. Chem. Res.* **2013**, *46* (8), 1900−1909.
(28) Meng, X. Y.; Li, J. J.; Liu, P.; Duan, M.; Wang, J.; Zhou, Y. N.; Xie, Y.; Luo, Z. H.; Pan, Y. X. Long-term stable hydrogen production from water and lactic acid via visible-light-driven photocatalysis in a porous microreactor. *Angew. Chem., Int. Ed.* **2023**, *62* (32), No. e202307490.
(29) Qi, M. Y.; Tang, Z. R.; Xu, Y. J. Near field scattering optical model-based catalyst design for artificial photoredox transformation. *ACS Catal.* **2023**, *13* (6), 3971−3982.
(30) Li, L.; Liu, G.; Qi, S.; Liu, X.; Gu, L.; Lou, Y.; Chen, J.; Zhao, Y. Highly efficient colloidal $Mn_xCd_{1-x}S$ nanorod solid solution for photocatalytic hydrogen generation. *J. Mater. Chem. A* **2018**, *6* (46), 23683−23689.
(31) Zhang, S.; Lou, J.; Wang, C.; Li, Q.; Li, Y.; Jin, L.; Guo, C. Modification strategies and applications of Mn−Cd−S solid solution-based photocatalysts. *Mater. Today Catal.* **2024**, *5*, 100055.
(32) Zhao, Q.; Sun, J.; Li, S.; Huang, C.; Yao, W.; Chen, W.; Zeng, T.; Wu, Q.; Xu, Q. Single nickel atoms anchored on nitrogen-doped graphene as a highly active cocatalyst for photocatalytic H_2 evolution. *ACS Catal.* **2018**, *8* (12), 11863−11874.
(33) Mao, C.; Zuo, F.; Hou, Y.; Bu, X.; Feng, P. In situ preparationof a Ti^{3+} self-doped TiO_2 film with enhanced activity as photoanode by N_2H_4 reduction. *Angew. Chem.* **2014**, *126*, 10653−10657.
(34) Guo, C.; Tian, K.; Wang, L.; Liang, F.; Wang, F.; Chen, D.; Ning, J.; Zhong, Y.; Hu, Y. Approach of fermi level and electron-trap level in cadmium sulfide nanorods via molybdenum doping with enhanced carrier separation for boosted photocatalytic hydrogen production. *J. Colloid Interface Sci.* **2021**, *583*, 661−671.
(35) Feng, T.; Zeng, Q.; Lu, S.; Yang, M.; Tao, S.; Chen, Y.; Zhao, Y.; Yang, B. Morphological and interfacial engineering of cobalt-based electrocatalysts by carbon dots for enhanced water splitting. *ACS Sustain. Chem. Eng.* **2019**, *7* (7), 7047−7057.
(36) Cheng, C.; Zhang, J.; Zeng, R.; Xing, F.; Huang, C. Schottky barrier tuning via surface plasmon and vacancies for enhanced photocatalytic H_2 evolution in seawater. *Appl. Catal. B Environ. Energy* **2022**, *310*, 121321.
(37) Tang, Y.; Xu, Z. F.; Sun, Y.; Wang, C.; Guo, Y.; Hao, W.; Tan, X.; Ye, J.; Yu, T. Simultaneous and efficient utilization of photogenerated electrons and holes: a case of single-atom Pd-anchored CdS twins. *Energy Environ. Sci.* **2024**, *17* (20), 7882−7894.
(38) Guo, Y.; Sun, J.; Tang, Y.; Jia, X.; Nie, Y.; Geng, Z.; Wang, C.; Zhang, J.; Tan, X.; Zhong, D.; Ye, J.; Yu, T. Efficient interfacial electron transfer induced by hollow-structured $ZnIn_2S_4$ for extending hot electron lifetimes. *Energy Environ. Sci.* **2023**, *16* (8), 3462−3473.
(39) Kresse, G.; Joubert, D. From ultrasoft pseudopotentials to the projector augmented-wave method. *Phys. Rev. B:Condens. Matter Mater. Phys.* **1999**, *59* (3), 1758−1775.
(40) Kresse, G.; Hafner, J. Ab initio molecular dynamics for liquid metals. *Phys. Rev. B:Condens. Matter Mater. Phys.* **1993**, *47* (1), 558−561.
(41) Kresse, G.; Furthmüller, J. Efficient iterative schemes for ab initio total-energy calculations using a plane-wave basis set. *Phys. Rev. B:Condens. Matter Mater. Phys.* **1996**, *54* (16), 11169−11186.
(42) Perdew, J. P.; Burke, K.; Ernzerhof, M. Generalized gradient approximation made simple. *Phys. Rev. Lett.* **1996**, *77* (18), 3865−3868.
(43) Monkhorst, H. J.; Pack, J. D. Special points for brillouin-zone integrations. *Phys. Rev. B:Condens. Matter Mater. Phys.* **1976**, *13* (12), 5188−5192.
(44) Nørskov, J. K.; Rossmeisl, J.; Logadottir, A.; Lindqvist, L.; Kitchin, J. R.; Bligaard, T.; Jónsson, H. Origin of the overpotential for oxygen reduction at a fuel-cell cathode. *J. Phys. Chem. B* **2004**, *108*, 17886−17892.
(45) Huo, D.; Kim, M. J.; Lyu, Z.; Shi, Y.; Wiley, B. J.; Xia, Y. One-dimensional metal nanostructures: from colloidal syntheses to applications. *Chem. Rev.* **2019**, *119* (15), 8972−9073.
(46) Shi, R.; Ye, H. F.; Liang, F.; Wang, Z.; Li, K.; Weng, Y.; Lin, Z.; Fu, W. F.; Che, C. M.; Chen, Y. Interstitial P-doped CdS with long-lived photogenerated electrons for photocatalytic water splittingwithout sacrificial agents. *Adv. Mater.* **2018**, *30*, 1705941.
(47) Guo, Y.; Sun, J.; Geng, Z.; Zhang, J.; Tan, X.; Ye, J.; Yu, T. Reinforced interfacial Cd−Se bond coupling photocatalytic hydrogen evolution with pyruvic acid synthesis. *Adv. Energy Mater.* **2024**, *14* (32), 2401285.
(48) Li, H.; Li, R.; Jing, Y.; Liu, B.; Xu, Q.; Tan, T.; Liu, G.; Zheng, L.; Wu, L. Z. S-scheme heterojunction/single-atom dual-driven charge transport for photocatalytic hydrogen production. *ACS Catal.* **2024**, *14* (10), 7308−7320.
(49) Tuinstra, F.; Koenig, J. L. Raman spectrum of graphite. *J. Chem. Phys.* **1970**, *53* (3), 1126−1130.
(50) Bai, X.; Wang, L.; Zhu, Y. Visible photocatalytic activity enhancement of $ZnWO_4$ by graphene hybridization. *ACS Catal.* **2012**, *2* (12), 2769−2778.
(51) Han, C.; Chen, Z.; Zhang, N.; Colmenares, J. C.; Xu, Y. J. Hierarchically CdS decorated 1D ZnO nanorods-2D graphene hybrids: low temperature synthesis and enhanced photocatalytic performance. *Adv. Funct. Mater.* **2015**, *25* (2), 221−229.
(52) Yan, X.; Xia, M.; Liu, H.; Zhang, B.; Chang, C.; Wang, L.; Yang, G. An electron-hole rich dual-site nickel catalyst for efficient photocatalytic overall water splitting. *Nat. Commun.* **2023**, *14* (1), 1741.
(53) Peng, W.; Liao, J.; Yan, Y.; Chen, L.; Ge, C.; Lin, S. Enriched nitrogen-doped carbon derived from expired drug with dual active sites as effective peroxymonosulfate activator: ultra-fast sulfamethoxazole degradation and mechanism insight. *Chem. Eng. J.* **2022**, *446*, 137407.
(54) Li, T.; Li, Y.; Guo, C.; Hu, Y. Dual-defect semiconductor photocatalysts for solar-to-chemical conversion: advances and challenges. *Chem. Commun.* **2024**, *60*, 2320−2348.
(55) Huang, J.; Chai, B.; Xiao, J.; Zhang, X.; Fan, G.; Song, G. Construction of 1D/3D $Co_9S_8/Mn_{0.3}Cd_{0.7}S$ Schottky heterojunction for dramatically boosted photocatalytic H_2 evolution performance. *Chem. Eng. J.* **2024**, *481*, 148501.
(56) He, X.; Zeng, D.; Liu, Y.; Chen, Q.; Yang, J.; Gao, R.; Fujita, T.; Wei, Y. Porous Co_xP nanosheets decorated $Mn_{0.35}Cd_{0.65}S$ nanoparticles for highly enhanced noble-metal-free photocatalytic H_2 generation. *J. Colloid Interface Sci.* **2022**, *625*, 859−870.
(57) Huang, Q.; Tao, Z.; Ye, L.; Yao, H.; Li, Z. $Mn_{0.2}Cd_{0.8}S$ nanowires modified by CoP_3 nanoparticles for highly efficient photocatalytic H_2 evolution under visible light irradiation. *Appl. Catal. B Environ. Energy* **2018**, *237*, 689−698.
(58) Ding, R.; Zhu, H.; Zhou, J.; Luo, H.; Xue, K.; Yu, L.; Zhang, Y. Highly water-stable and efficient hydrogen-producing heterostructure synthesized from $Mn_{0.5}Cd_{0.5}S$ and a zeolitic imidazolate framework ZIF-8 via ligand and cation exchange. *ACS Appl. Mater. Interfaces* **2023**, *15* (30), 36477−36488.
(59) Xia, X.; Zhao, G.; Yan, Q.; Wang, B.; Wang, Q.; Xie, H. High-density defects activating Fe-doped molybdenum sulfide@N-doped carbon heterostructures for efficient electrochemical hydrogen evolution. *ACS Appl. Mater. Interfaces* **2022**, *10* (1), 182−193.
(60) Gu, J.; Yuan, Z.; Wang, H.; Shen, J.; Ning, J.; Zhong, Y.; Hu, Y. Local protonation of polyaniline induced by nitrogen-doped carbon skeleton towards ultra-stable Zn-organic batteries with a dual-ion insertion/extraction mechanism. *Chem. Eng. J.* **2022**, *448*, 137711.
(61) Hao, Q.; Zhong, H. X.; Wang, J. Z.; Liu, K. H.; Yan, J. M.; Ren, Z. H.; Zhou, N.; Zhao, X.; Zhang, H.; Liu, D. X.; Liu, X.; Chen, L. W.; Luo, J.; Zhang, X. B. Nickel dual-atom sites for electrochemicalcarbon dioxide reduction. *Nat. Synth.* **2022**, *1*, 719−728.

(62) Xie, Z.; Luo, H.; Xu, S.; Li, L.; Shi, W. Proton turnover dominated cascade route for CO_2 photoreduction. *Adv. Funct. Mater.* **2024**, *34* (17), 2313886.
(63) Jin, X.; Wang, R.; Zhang, L.; Si, R.; Shen, M.; Wang, M.; Tian, J.; Shi, J. Electron configuration modulation of nickel single atoms for elevated photocatalytic hydrogen evolution. *Angew. Chem.* **2020**, *132*, 6894−6898.
(64) Zhu, X.; Zong, H.; Pérez, C. J. V.; Miao, H.; Sun, W.; Yuan, Z.; Wang, S.; Zeng, G.; Xu, H.; Jiang, Z.; Ozin, G. Supercharged CO_2 photothermal catalytic methanation: high conversion, rate, and selectivity. *Angew. Chem., Int. Ed.* **2023**, *62*, No. e202218694.
(65) Qureshi, M.; Takanabe, K. Insights on measuring and reporting heterogeneous photocatalysis: efficiency definitions and setup examples. *Chem. Mater.* **2017**, *29* (1), 158−167.
(66) Cao, S.; Piao, L. Considerations for a more accurate evaluation method for photocatalytic water splitting. *Angew. Chem., Int. Ed.* **2020**, *59* (42), 18312−18320.
(67) Wang, Z.; Hisatomi, T.; Li, R.; Sayama, K.; Liu, G.; Domen, K.; Li, C.; Wang, L. Efficiency accreditation and testing protocols for particulate photocatalysts toward solar fuel production. *Joule* **2021**, *5* (2), 344−359.
(68) Li, H.; Li, R.; Jing, Y.; Liu, B.; Xu, Q.; Tan, T.; Liu, G.; Zheng, L.; Wu, L. Z. S-scheme heterojunction/single-atom dual-driven charge transport for photocatalytic hydrogen production. *ACS Catal.* **2024**, *14* (10), 7308−7320.
(69) Li, Y.; Yu, S.; Xiang, J.; Zhang, F.; Jiang, A.; Duan, Y.; Tang, C.; Cao, Y.; Guo, H.; Zhou, Y. Revealing the importance of hole transfer: boosting photocatalytic hydrogen evolution by delicate modulation of photogenerated holes. *ACS Catal.* **2023**, *13* (12), 8281−8292.
(70) Han, C.; Xiang, S.; Jin, S.; Zhang, C.; Jiang, J. X. Rational design of conjugated microporous polymer photocatalysts with definite D−π−A structures for ultrahigh photocatalytic hydrogen evolution activity under natural uunlight. *ACS Catal.* **2023**, *13* (1), 204−212.
(71) Xu, T.; Su, X.; Zhu, Y.; Khan, S.; Chen, D. L.; Guo, C.; Ning, J.; Zhong, Y.; Hu, Y. One-pot solvothermal synthesis of flower-like Fe-doped In_2S_3/Fe_3S_4 S-scheme hetero-microspheres with enhanced interfacial electric field and boosted visible-light-driven CO_2 reduction. *J. Colloid Interface Sci.* **2023**, *629*, 1027−1038.
(72) Cui, B.; Lin, H.; Liu, Y. Z.; Li, J. b.; Sun, P.; Zhao, X.; Liu, C. j. Photophysical and photocatalytic properties of core-ring structured $NiCo_2O_4$ nanoplatelets. *J. Phys. Chem. C* **2009**, *113* (32), 14083−14087.
(73) Liang, Z.-H.; Wang, J.; Wang, D.; Zhou, J. Z.; Wu, D. Y. Effects of traps on photo-induced interfacial charge transfer of Ag-TiO_2: photoelectrochemical, electrochemical and spectroscopic characterizations. *J. Electrochem.* **2023**, *29* (8), 2208101.
(74) Wang, H.; Wang, X.; Hu, P.; Liu, T.; Weng, B.; Ye, K.; Luo, Y.; Ji, H. Vacancy pair induced surface chemistry reconstruction of $Cs_2AgBiBr_6/Bi_2WO_6$ heterojunction to enhance photocatalytic CO_2 reduction. *Appl. Catal. B Environ. Energy* **2024**, *351*, 123956.
(75) Pan, A.; Ma, X.; Huang, S.; Wu, Y.; Jia, M.; Shi, Y.; Liu, Y.; Wangyang, P.; He, L.; Liu, Y. $CsPbBr_3$ perovskite nanocrystal grown on MXene nanosheets for enhanced photoelectric detection and photocatalytic CO_2 reduction. *J. Phys. Chem. Lett.* **2019**, *10* (21), 6590−6597.
(76) Zhang, N.; Jalil, A.; Wu, D.; Chen, S.; Liu, Y.; Gao, C.; Ye, W.; Qi, Z.; Ju, H.; Wang, C.; Wu, X.; Song, L.; Zhu, J.; Xiong, Y. Refining defect states in $W_{18}O_{49}$ by Mo doping: a strategy for tuning N_2 activation towards solar-driven nitrogen fixation. *J. Am. Chem. Soc.* **2018**, *140* (30), 9434−9443.
(77) Wang, S.; He, T.; Chen, P.; Du, A.; Ostrikov, K.; Huang, W.; Wang, L. In situ formation of oxygen vacancies achieving near-complete charge separation in planar $BiVO_4$ photoanodes. *Adv. Mater.* **2020**, *32* (26), 2001385.
(78) Xiao, Y.; Sun, Q.; Leng, J.; Jin, S. Time-resolved spectroscopy for dynamic investigation of photoresponsive metal−organic frameworks. *J. Phys. Chem. Lett.* **2024**, *15* (12), 3390−3403.
(79) He, B.; Wang, Z.; Xiao, P.; Chen, T.; Yu, J.; Zhang, L. Cooperative coupling of H_2O_2 production and organic synthesis over a floatable polystyrene-sphere-supported TiO_2/Bi_2O_3 S-scheme photocatalyst. *Adv. Mater.* **2022**, *34* (38), 2203225.
(80) Li, M.; Yang, Y.; Kuang, Z.; Hao, C.; Wang, S.; Lu, F.; Liu, Z.; Liu, J.; Zeng, L.; Cai, Y.; Mao, Y.; Guo, J.; Tian, H.; Xing, G.; Cao, Y.; Ma, C.; Wang, N.; Peng, Q.; Zhu, L.; Huang, W.; Wang, J. Acceleration of radiative recombination for efficient perovskite LEDs. *Nature* **2024**, *630* (8017), 631−635.
(81) Xiao, Y.; Liu, J.; Leng, J.; Yin, Z.; Yin, Y.; Zhang, F.; Sun, C.; Jin, S. Long-lived internal charge-separated state in two-dimensional metal−organic frameworks improving photocatalytic performance. *ACS Energy Lett.* **2022**, *7* (7), 2323−2330.
(82) Xiao, Y.; Feng, C.; Fu, J.; Wang, F.; Li, C.; Kunzelmann, V. F.; Jiang, C. M.; Nakabayashi, M.; Shibata, N.; Sharp, I. D.; Domen, K.; Li, Y. Band structure engineering and defect control of Ta_3N_5 for efficient photoelectrochemical water oxidation. *Nat. Catal.* **2020**, *3* (11), 932−940.
(83) Meng, J.; Lee, C.; Li, Z. Adjustment methods of schottky barrier height in one- and two-dimensional semiconductor devices. *Sci. Bull.* **2024**, *69* (9), 1342−1352.
(84) Meng, X.; Wang, S.; Zhang, C.; Dong, C.; Li, R.; Li, B.; Wang, Q.; Ding, Y. Boosting hydrogen evolution performance of a CdS-based photocatalyst: in situ transition from type I to type II heterojunction during photocatalysis. *ACS Catal.* **2022**, *12* (16), 10115−10126.
(85) Li, L.; Guo, C.; Shen, J.; Ning, J.; Zhong, Y.; Hu, Y. Construction of sugar-gourd-shaped $CdS/Co_{1-x}S$ hollow hetero-nanostructure as an efficient Z-scheme photocatalyst for hydrogen generation. *Chem. Eng. J.* **2020**, *400*, 125925.
(86) Liao, Y. W.; Yang, J.; Wang, G. H.; Wang, J.; Wang, K.; Yan, S. D. Hierarchical porous NiO as a noble-metal-free cocatalyst for enhanced photocatalytic H_2 production of nitrogen-deficient g-C_3N_4. *Rare Met.* **2022**, *41* (2), 396−405.

https://doi.org/10.1021/acscatal.4c06476
ACS Catal. 2025, 15, 2315−2327